Supplemental Information

Materials and Methods:

Strains and plasmids construction

Standard methods for the growth, maintenance and transformation of yeast and bacteria and for manipulation of DNA were used throughout. The yeast strains used in this study were generated from BY4741 (*MAT a his3Δ1 leu2Δ0 met15Δ0 ura3Δ0*) strain background. Strain and plasmid information is provided in Tables S1 and S2.

To make the nuclear reporter for single cells, a *IRFP::KanMX* fragment was PCR amplified and integrated into the C-terminus of *NHP6a* at the native locus by homolog recombination. To make *sir2Δ* mutants, a *CgHIS3*(1) fragment was amplified to replace the *SIR2* open reading frame by homolog recombination. Similarly, the *SGF73* ORF was replaced with *CgHIS3*. The *URA3* ORF is deleted in the BY4741 background. To add a mutated *URA3* gene (*ura3-1*) back to its native locus, a *CgURA3* fragment (1) was amplified and inserted at *URA3*, then *CgURA3* was replaced with a *ura3-1* allele from the W303 strain.

To make the *NTS1* silencing reporter, a *Xho*1-*NTS1*-*Eco*RI fragment from pDM704 (2) was ligated into the pRS306 plasmid vector. A *Eco*RI-P_{TDH3}-*GFP*-*Eag*I fragment contains 680 bp of *TDH3* promoter and *GFP* ORF was made by fusion PCR and then ligated into pRS306 and the plasmid pRS306 with *Xho*1-*NTS1*-*Eco*RI fragment to get plasmids NHB0206 and NHB0200. Plasmids NHB0213 and NHB0214 were constructed in the same way. The *NTS2* fragment for plasmid NHB0214 was derived from plasmid pDM312(2). Yeast strains with rDNA silencing reporter were generated by transformation with NHB0200 cut with *Hind*III to integrate at *NTS1*, NHB0213 cut with *Hind*III to integrate at *NTS1*, NHB0214 cut with *Sma*I to integrate at *NTS2*, and NHB0206 cut with *Stu*I to integrate at *ura3-1*. All transformations were performed with the lithium acetate method (3), and integration was confirmed by PCR.

Quantification of bud scar numbers

Yeast cells were inoculated into 2 ml of synthetic complete medium (SC, 2% dextrose) and cultured overnight at 30°C. 2 μl of saturated culture was diluted into 20 ml of fresh SC medium and grown at 30°C overnight. To evaluate the bud scar distribution of yeast cells, a cell culture with OD600 ~ 1.0 was sampled and stained with 5 μg/ml WGA conjugates (Alexa Fluor 647 conjugate, Thermo Fisher) for 10 min at 37°C. Cells were washed twice with PBS after incubation then examined with a Leica TCS SP8 Stimulated Emission Depletion (STED) super-resolution microscope using a Cy5.5 channel to visualize the bud scars.

Design and fabrication of the microfluidic device for yeast aging studies

In designing a microfluidic device for studying aging in budding yeast, the viability of the cells, efficiency of cell trapping and robustness of the device were our primary concerns. Multiple designs were built and tested to optimally satisfy these criteria. The robustness of the device is affected by clogging due to excess cells around the traps and at the waste port, which can interfere with mother cell lifespan and retention. Supplying media through ~20 μm tall main channels readily allowed excess cells to be washed away and prevented clogging. Therefore, a critical feature of our device is its two-layer design, making it extremely robust over the course of our experiments that takes more than 80 hours. This is a unique feature compared to recently

published devices that are all single-layer (4-6). The device was optimized for using continuous gravity-driven flow during operation, with the three-inlet design also facilitating media switching experiments. The height and width of cell traps were optimized for cell loading and retention. Cell loading efficiencies and final retentions until cell death are approximately 93% and 75% respectively. See ***Quantification of single-cell traces*** below for a consideration of cell retention**.** We quantified the widths of cells in the culture population immediately before loading and cells that are just loaded into the device, respectively. As shown in Fig. S1B, the distributions of cell widths are similar for the population before loading and for the loaded population, confirming that the device loading does not select for a subpopulation of cells. A potential caveat of microfluidic devices for aging studies is that the limited size of cell traps might affect the lifespan. However, given that lifespans measured using our device are comparable to those from classical microdissection studies (Fig. S1C), the effect of the trap size on lifespan, if any, should be modest.

To construct the microfluidic device, designs were first drawn in AutoCAD (Autodesk Inc.). Modeling of fluid flow in the device using COMSOL Multiphysics aided in design (COMSOL Inc.). Two chrome quartz glass masks (HTA Photomask), one for each layer of the device, were used to pattern SU-8 negative epoxy photoresist (MicroChem Corp.) onto clean silicon wafers (University Wafer Inc.). SU-8 2005 was used to build the first layer (cell trapping region) and was spun at 3250 rpm while SU-8 2015 was used to build the second layer (main channels), spun at 2000 rpm. These spin parameters yield approximately 4.3 μm and 20 μm tall features for the cell trapping and main channel layers respectively, as measured by a Dektak 150 surface profiler (Veeco Instruments Inc.). The mask for the second layer was aligned to the first layer of the wafer using an EVG620 mask aligner (EV Group Inc.). Once patterning of the SU-8 was complete, the wafer was exposed to 40 μl of trichloro(1H, 1H, 2H, 2H-perfluoro-octyl)silane (Sigma-Aldrich Co.) in a vacuum chamber for 7 minutes. After this, poly-dimethylsiloxane (PDMS, Sylgard 184, silicone elastomer kit with base and curing agent, Dow Corning Corp.) molds of the features on the wafer were made, cleaned and bonded to glass coverslips for experiments as described in (7).

Setting up a microfluidics experiment

Each microfluidic device was checked carefully before use to ensure no dust or broken features were present. Before setting up a microfluidics experiment, the device was vacuumed for 20 min. After vacuum, all of the inlets of the device were covered with 0.075% Tween 20 (Sigma-Aldrich Co.) for 5 min. The microfluidic device was placed on the stage of an inverted microscope with a 30°C incubator system. Three media ports were connected to plastic tubing, which connected to 60 ml syringes with fresh SC medium containing 0.04% Tween-20. The height of all three medium syringes is about 20 inches above the stage. The waste port of the microfluidic device was connected to plastic tubing, which was set to stage height. Yeast cells were inoculated into 2 ml of synthetic complete medium (SC, 2% dextrose) and cultured overnight at 30°C. 2 μl of saturated culture was diluted into 20 ml of fresh SC medium and grown at 30°C overnight until it reached $OD600_{nm}$ ~ 1.0. For loading, cells were diluted by 10-fold and transferred into a 60 ml syringe (Luer-Lok Tip, BD) connected to plastic tubing (TYGON, ID 0.020 IN, OD 0.060 IN, wall 0.020 IN). To load cells, the connected syringe on the middle port was replaced with a syringe filled with yeast culture. The height of the cell-loading syringe is also about 20 inches above the stage. The flow of medium in the device was

maintained by gravity and drove cells into traps. Most traps were filled with cells within 2-5 minutes, after which cell loading tubing was replaced with media supply tubing and syringe as above. Then the height of all medium tubing and the waste tubing were adjusted to make the height difference around 60 inches. Waste medium was collected in a 50 ml tube to measure flow rate, which was about 2.5 ml/day.

For experiments with media switching, left and right medium ports were connected to syringes with fresh SC medium containing 0.04% Tween-20 and the middle medium port was connected to a syringe containing medium with NA or NAM and 0.1 μg/ml Atto 655 cy5 dye (Sigma 93711). The waste port of the microfluidic device was connected to plastic tubing set to a position about 20 inches below the stage. Before cell loading, the heights of syringes need to be calibrated for media switching. Syringes connected to the left and right medium ports were moved to the same height as the microscope stage and the syringe containing NA or NAM was moved to about 33 inches above the stage. To further calibrate the positions, the junction of all three media channels was imaged under the cy5 channel and the positions of syringes were adjusted to ensure the cell trapping region was fully filled with the NA or NAM medium. The position of all syringes were marked and used for NA or NAM during the experiment. To switch from the NA or NAM medium to SC medium, the left and right syringes were moved to about 33 inches above the stage and the middle syringes was moved to the same height as the stage. The positions of all syringes were further calibrated under the cy5 channel to ensure only SC medium went into the cell trapping region and then marked the positions of all syringes for the condition of no NA or NAM in the cell culture chamber. Cell loading was as for experiments without media switching. After cell loading, all syringes were moved to previously marked positions. The flow rate is about 2.5 ml/day.

We note that Tween-20 is a non-ionic surfactant capable of coating the hydrophobic PDMS surface of microfluidic devices, thereby reducing protein interactions and cell friction on the PDMS (8, 9). We have used Tween-20 or Tween-80 at very low concentrations in all the microfluidic experiments for more than 10 years on a variety of organisms including budding yeast (10-16) without any adverse effects on cells. We have found that Tween-20 aids in preventing clogs and air bubbles from forming and therefore helps with the robustness and reproducibility of microfluidics experiments (7). We have observed no difference in the cell doubling times in media with or without Tween-20 and have obtained lifespan measurements using our microfluidics setup that are comparable to values in the literature (for WT and mutants; Fig. S1C), confirming that Tween-20 has no significant effect on lifespan or physiology.

Time-lapse microscopy

Time-lapse microscopy experiments were performed using a Nikon Ti-E inverted fluorescence microscope with Perfect Focus, coupled with an EMCCD camera (Andor iXon X3 DU897). The light source is a spectra X LED system. Images were taken using a CFI plan Apochromat Lambda DM 60X oil immersion objective (NA 1.40 WD 0.13MM). During experiments, the microfluidic device was taped to a customized device holder inserted onto the motorized stage (with Encoders). In all experiments, the microscope was programmed to acquire images for each fluorescence channel every 15 min for a total of 80 hours or more. The exposure and intensity setting for each channel were set as follows: Phase 50 ms, GFP 10 ms at 10% lamp intensity with an EM Gain of 50, mCherry 50 ms at 10% lamp intensity with an EM Gain of 200, and iRFP 300

ms at 15% lamp intensity with an EM Gain of 300. The EM Gain settings are within the linear range. We confirmed that this fluorescence imaging setting did not affect lifespan (Fig. S1D).

Quantification of single-cell traces

Fluorescence images were processed with a custom MATLAB code. Background of images from each channel was subtracted. Cell nuclei were identified by thresholding the iRFP images. Each image was evenly divided into 6 parts, each containing a single cell trap. The position of the dent in the cell trap was labeled. In each trap, the positions of all nuclei of each single cell were labeled. Mother cells are identified by comparing the positions of the dent and the positions of nuclei. Since the fluorescence reporter of rDNA silencing is evenly distributed inside the cell, nuclei of mother cells were further dilated to generate a mask to quantify the intensities of fluorescence reporters. The mean intensity value of the top 50% pixels of fluorescence reporter is used as the intensity of the rDNA silencing reporter. All single-cell time traces were normalized by the mean reporter intensity of WT cells' 1^{st} cell cycle and smoothed with local regression using weighted linear least squares and a 2^{nd} degree polynomial model. The normalized and smoothed data were used for plotting of trajectories and density maps.

We also tested segmenting the whole cell using phase images and quantified the mean fluorescence intensities of the whole cell. The resulting time traces were similar to those obtained using nuclei segmentation and quantification as described above. Because nuclei segmentation and quantification is more robust than whole cell segmentation and allows us to identify and analyze more cells automatically, we used the former method for all imaging analysis.

Cell divisions of each mother cell were manually identified and counted at the time that the nuclei separated between mother and daughter cells. Cells were categorized based on their aging phenotypes, characterized by the morphologies of later daughters they produced. Mothers continually producing elongated daughters at the last few generations were categorized as "cells aging with elongated daughters", whereas mothers continually producing round daughters at the last few generations were categorized as "cells aging with rounded daughters." A small fraction of cells show abnormal morphologies even at the very beginning of the experiment and have a lifespan shorter than 5 generations. Those cells were excluded from analysis.

To identify the peaks and troughs of silencing loss pulses for aging cells, we first took the time derivative of the fluorescence trajectory of each single cell and then digitalized the curve by setting positive derivatives as 1 and negative derivatives as -1. The time points with the derivative transition from -1 to 1 were identified as "troughs" and the time points with the derivative transition from 1 to -1 were identified as "peaks". This identification process is illustrated in Fig. S4B.

During aging experiments, about 25% of mother cells escaped from chambers before their final death. The major reason for a mother cell to escape from the chamber is that when the mother produces a daughter cell toward the bottom of the chamber, depending on the bud position, occasionally the daughter cell will not go through the small opening at the bottom of the chamber. Instead, the daughter will stay in the chamber and push the mother out. We observed that the times that these cells escaped were randomly distributed throughout the experiments. We further

quantified the silencing time traces of these escaped cells. During their time in the device, all of the escaped cells showed intermittent silencing loss dynamics with no obvious difference to those presented in Fig. 2. The data from escaped cells have been excluded from further analysis or presentation in this work.

Correlation analysis of single-cell data

Correlation coefficients (R) for all the scatter plots were calculated using the MATLAB function: 'corrcoef.'

To determine the time-dependent relationship between silencing loss in aging mother cells and the occurrence of elongated daughters, we calculated the cross-correlation between silencing reporter fluorescence trajectories of each mother cell (from Fig. 2A) and the morphology change trajectories of its daughters.

The daughter morphology was mapped as a binary variable that is set to "1" when the daughter is elongated and "0" when the daughter is rounded. Because daughter morphology traces are digitalized, we also digitized silencing reporter fluorescence trajectories of mother cells. To this end, we first took the time derivatives of a fluorescence trajectory, and then set positive derivatives as 1 (representing the silencing loss state) and negative derivatives as -1 (representing the silenced state).

For each pair of mother silencing loss trajectory, $M_{SL}(1, 2, \ldots n)$, and daughter morphology trace i, $D_M(1, 2, \ldots n)$, with n time points, we aligned them with a time shift $\Delta\tau$: $M_{SL(i)}(1, 2, \ldots n\text{-}\Delta\tau)$ and $D_{M(i)}(1+\Delta\tau, 2+\Delta\tau, \ldots n)$ for $\Delta\tau \geq 0$, or $M_{SL(i)}(1+|\Delta\tau|, 2+|\Delta\tau|, \ldots n)$ and $D_{M(i)}(1, 2, \ldots n-|\Delta\tau|)$ for $\Delta\tau < 0$. For each $\Delta\tau$, we concatenated all mother silencing loss trajectories into one long silencing loss trajectory and all daughter morphology trajectories into one long morphology trajectory. We then calculated the correlation coefficient between the concatenated pair of mother-daughter trajectories with the shift $\Delta\tau$ using Matlab function corrcoef.

To provide a control for this cross correlation analysis, we disrupted the original pairing between mother silencing loss and daughter morphology trajectories. Instead of pairing each mother silencing loss trajectory with its own daughter morphology trajectory, we randomly paired mother silencing loss trajectories with daughter morphology trajectories, and then performed the same cross correlation calculation for the concatenated mother trajectory and "randomly reshuffled" daughter trajectory (the dash line in Fig. S2).

The correlation analysis revealed a ~140 min time lag between silencing loss and daughter morphology trajectories, indicating a ~140 min time delay between the changes at the molecular level – the occurrence of silencing loss and the changes at the phenotypic level – the production of elongated daughters during the aging process.

Development of the phenomenological model of cell aging

We developed a phenomenological model that relates silencing and cell aging based on our experimental data. The model only considers the aging process with elongated daughters and postulates that each mother cell can be in one of two states during aging: state 0 – the silencing

state in which it produces normal daughters, and state 1 – the silencing loss state with elongated daughters, and a cell may only die from state 1 (Fig. 4A).

The transitions between the states are purely stochastic and are characterized by transition probabilities p_{01} and p_{10} that depend on the replicative age of the cell. All the experimental data are from Fig. 2A. Due to the phenomenological nature of the model, we only used the age-dependent phenotypic change (elongated daughter) data for model fitting. To deduce the transition probabilities from the single-cell data, we computed the fraction of all the cells at the state with normal daughters (state 0) of a given generation that switch to the state with elongated daughters (state 1) at the next cell cycle ($f_{0->1}$) and the fraction of the cells at the state with elongated daughters (state 1) that return to state 0 at the next cell cycle ($f_{1->0}$), as a function of the replicative age. As this data shows, the transition rate from state 0 to state 1 gradually increases with age, while the rate of the reverse process decreases and reaches zero after ~25 generations (Fig. 4B). Using linear regression of the data, we approximate the dependence of p_{01} and p_{10} on the replicative age n by linear functions, $p_{01}(n) = 0.016 \cdot n$-0.04 and $p_{10}(n) = 0.27 - 0.01 \cdot n$.

We also postulate that in the silencing loss state (state 1), a damage factor D accumulates continuously, and the probability of a cell to die is proportional to D. To obtain the relationship between damage accumulation and cell death, we calculated the fraction $f_{1\to D}$ of cells that died after N consecutive generations in state 1 to total number of cells that lived through N consecutive generations in state 1 (Fig 4C). Evidently, this fraction becomes higher with N, however at large N>10 the data becomes very noisy since only small number of cells remain living. We use the data for N<10 to approximate the probability of transition to death from state 1 by a linear function of N, $p_{1D}(N) = 0.0297 \cdot N$+0.00025 and used this expression for all N. We assume that the damage D is proportional to the time the cell spent in state 1 and, once a cell transits back to the silencing state 0, D is reset to zero.

Thus, the phenomenological model depends on two transition rates p_{01} and p_{10} that are linear functions of the generation number n, and the death rate p_{1D} that is a linear function of the number of consecutive generations in state 1. Time unit in simulations is one generation. Based on the experimental data we set one generation in the silencing state is 80 min, and in the silencing loss state, 110 min. We simulated this model stochastically and in each *in silico* experiment we generated 79 cell state trajectories (same number as cells in experimental data in Fig. 2A). Using these data and averaging over 200 *in silico* experiments, we computed the number of cells alive at replicative age n as a function of n (Fig. 4D, red line), the fraction of cells in state 1 as a function of their replicative age (Fig. 4E, red line), and the distribution of continuous generations in state 1 before death (Fig. 4F, red line). The error bars indicate standard deviations of the distribution for the corresponding results from multiple runs. All these simulation results match our experimental data very well. We also plotted the individual cell trajectories from one *in silico* run ordered according to the replicative lifespan (Fig. 4G).

To simulate the effects of silencing perturbations, we increased p_{01} and decreased p_{10} by ten-fold to generate an induced silencing loss, see Fig. 4H. To simulate the transient silencing loss

(Fig. 4I), we used the same high p_{01} and low p_{10} as in Fig. 4H at the beginning of simulation for 4 generations then switch them back to the p_{01} and p_{10} used in Fig. 4G. We have included the MATLAB code for simulation as Code S1.

Table S1. Strains used or constructed in this study.

Strain Name	Description
NH0256	*BY4741 MAT*a *his3Δ1 leu2Δ0 met15Δ0 ura3Δ0*
NH0268	*BY4741 MAT*a *his3Δ1 leu2Δ0 met15Δ0 ura3Δ0, NHP6a-iRFP-kanMX*
NH0270	*BY4741 MAT*a *his3Δ1 leu2Δ0 met15Δ0 ura3Δ0, RDN1::NTS1-*P_{TDH3}*-GFP, NHP6a-iRFP-kanMX*
NH0273	*BY4741 MAT*a *his3Δ1 leu2Δ0 met15Δ0, NHP6a-iRFP-kanMX, ura3Δ0::ura3-1*
NH0277	*BY4741 MAT*a *his3Δ1 leu2Δ0 met15Δ0 ura3Δ0, NHP6a-iRFP-kanMX, RDN1::NTS1-*P_{TDH3}*-GFP-URA3, sir2::HIS3*
NH0321	*BY4741 MAT*a *his3Δ1 leu2Δ0 met15Δ0 ura3Δ0, NHP6a-iRFP-kanMX, RDN1::NTS1-*P_{TDH3}*-GFP-URA3, RDN1::NTS2-*P_{TDH3}*-mCherry-LEU2*
NH0322	*BY4741 MAT*a *his3Δ1 leu2Δ0 met15Δ0, NHP6a-iRFP-kanMX, RDN1::NTS1-*P_{TDH3}*-mCherry-LEU2, ura3-1::URA3-*P_{TDH3}*-GFP*
NH0465	*BY4741 MAT*a *his3Δ1 leu2Δ0 met15Δ0 ura3Δ0, NHP6a-iRFP-kanMX, RDN1::NTS1-*P_{TDH3}*-GFP-URA3, sgf73::HIS3*

Table S2. Plasmids constructed in this study.

Plasmid Name	Description
NHB0200	pRS306_XhoI_NTS1_EcoRI_P_{GPD}-GFP_EagI
NHB0206	pRS306_EcoRI_P_{GPD}-GFP_EagI
NHB0213	pRS305_ApaI_NTS1-P_{GPD}-mCherry_SacI
NHB0214	pRS305_ApaI_NTS2-P_{GPD}-mCherry_SacI

Code S1. The MATLAB code used to generate simulations in Fig. 4G-I.

Figures S1 - 8

References

1. Kitada K, Yamaguchi E, & Arisawa M (1995) Cloning of the Candida glabrata TRP1 and HIS3 genes, and construction of their disruptant strains by sequential integrative transformation. *Gene* 165(2):203-206.
2. Huang J & Moazed D (2003) Association of the RENT complex with nontranscribed and coding regions of rDNA and a regional requirement for the replication fork block protein Fob1 in rDNA silencing. *Genes & development* 17(17):2162-2176.
3. Gietz RD & Schiestl RH (2007) Quick and easy yeast transformation using the LiAc/SS carrier DNA/PEG method. *Nat Protoc* 2(1):35-37.
4. Crane MM, Clark IB, Bakker E, Smith S, & Swain PS (2014) A microfluidic system for studying ageing and dynamic single-cell responses in budding yeast. *PloS one* 9(6):e100042.
5. Jo MC, Liu W, Gu L, Dang W, & Qin L (2015) High-throughput analysis of yeast replicative aging using a microfluidic system. *Proc Natl Acad Sci U S A* 112(30):9364-9.
6. Liu P, Young TZ, & Acar M (2015) Yeast Replicator: A High-Throughput Multiplexed Microfluidics Platform for Automated Measurements of Single-Cell Aging. *Cell reports* 13(3):634-644.
7. Ferry MS, Razinkov IA, & Hasty J (2011) Microfluidics for synthetic biology: from design to execution. *Methods Enzymol* 497:295-372.
8. Wong I & Ho CM (2009) Surface molecular property modifications for poly(dimethylsiloxane) (PDMS) based microfluidic devices. *Microfluid Nanofluidics* 7(3):291-306.
9. Boxshall K*, et al.* (2006) Simple surface treatments to modify proteinadsorption and cell attachment properties within apoly(dimethylsiloxane) micro-bioreactor. *Surf Interface Anal* (38):198-201.
10. Cookson S, Ostroff N, Pang WL, Volfson D, & Hasty J (2005) Monitoring dynamics of single-cell gene expression over multiple cell cycles. *Mol Syst Biol* 1:2005 0024.
11. Stricker J*, et al.* (2008) A fast, robust and tunable synthetic gene oscillator. *Nature* 456(7221):516-519.
12. Danino T, Mondragon-Palomino O, Tsimring L, & Hasty J (2010) A synchronized quorum of genetic clocks. *Nature* 463(7279):326-330.
13. Mondragon-Palomino O, Danino T, Selimkhanov J, Tsimring L, & Hasty J (2011) Entrainment of a population of synthetic genetic oscillators. *Science* 333(6047):1315-1319.
14. Prindle A*, et al.* (2011) A sensing array of radically coupled genetic 'biopixels'. *Nature* 481(7379):39-44.
15. Baumgartner BL*, et al.* (2011) Antagonistic gene transcripts regulate adaptation to new growth environments. *Proc Natl Acad Sci U S A* 108(52):21087-21092.
16. Luke CS*, et al.* (2016) A Microfluidic Platform for Long-Term Monitoring of Algae in a Dynamic Environment. *ACS Synth Biol* 5(1):8-14.

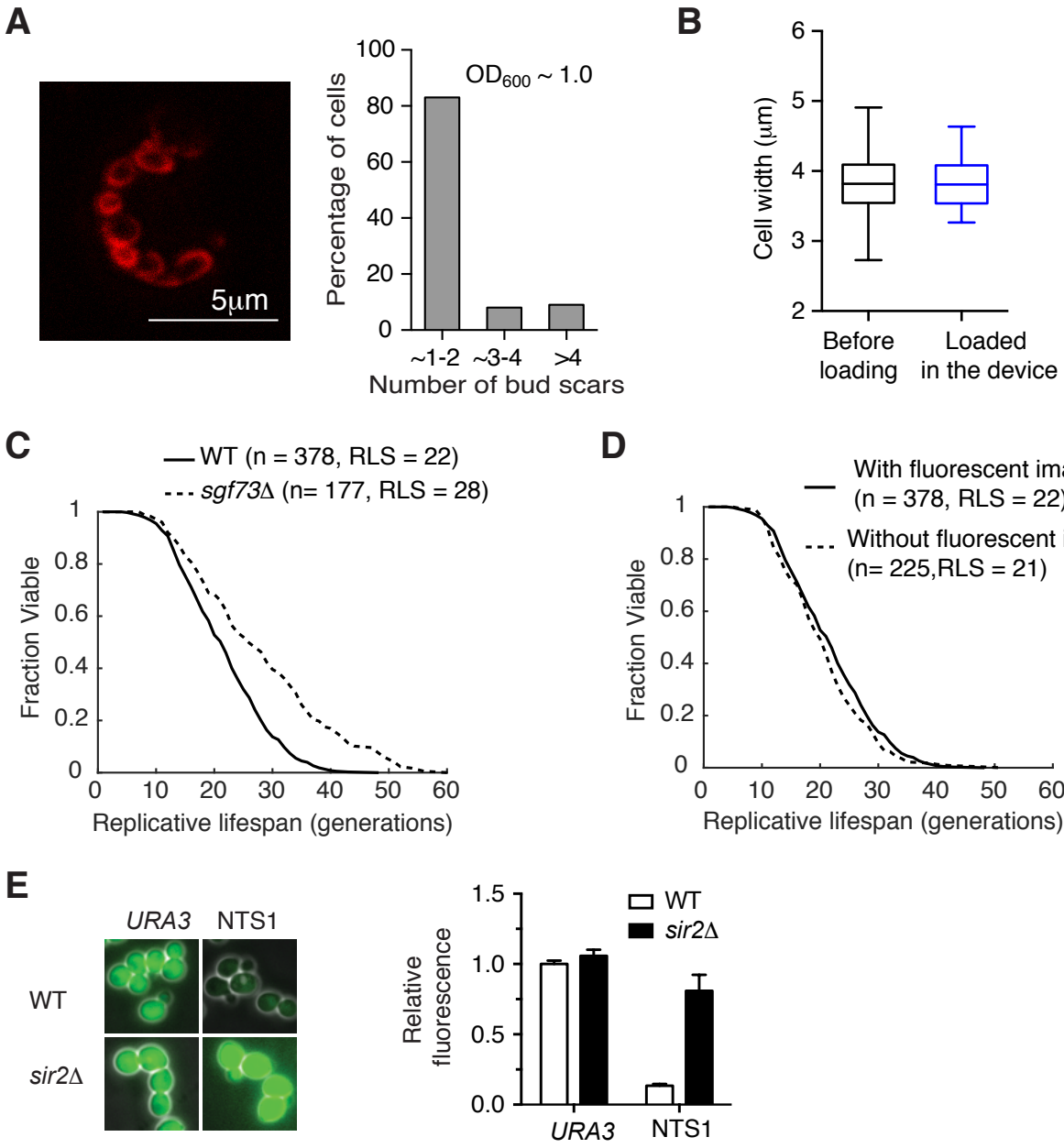

Fig. S1. Validation of the technologies - the microfluidic device and the silencing reporter. (A) Left: A representative confocal image showing bud scars stained with wheat germ agglutinin (WGA). Right: Bud scar distribution of cells at OD600 ~ 1.0. Cells with OD600 ~ 1.0 from the same culturing procedure (see SI: Setting up a microfluidics experiment) have been consistently used to load the device throughout our work. **(B)** A boxplot showing the distributions of cell widths for cells from the culture population before loading (black) and cells loaded in the device (blue). Snapshot images were taken with cells from the culture population immediately before loading or with cells just loaded into the device, respectively. Cell widths for single cells were quantified using ImageJ. In the plot, the bottom and top of the box are first (the 25th percentile of the data, q1) and third quartiles (the 75th percentile of the data, q3); the band inside the box is the median; the whiskers cover the range between q1-1.5 x (q3-q1) and q3+1.5 x (q3-q1). These results confirm that the device loading does not select for a subpopulation of cells.(**C**) Replicative lifespans measured using the microfluidic device. Lifespan curves have been shown for WT and *sgf73*Δ cells in SC medium supplemented with 2% glucose. In our device, deletion of *SGF73* increases lifespan by 27% comparing to that of WT, consistent with the previouse reprot (McCormick et al, *Cell Metabolism* 2015, Table S2; the *sgf73* mutant increases lifespan by 25.8% in *MAT*a strains). (**D**) Replicative lifespans measured in the device with or without fluorescent imaging. Fluorescent imaging setting and acquisition frequency have been provided in SI: Time-lapse microscopy. For experiments without fluorescent imaging, only phase images (50 ms exposure) were taken every 15 mins. **(E)** Validation of the reporter. Left: Representative images of WT or *sir2*Δ cells with the fluorescence reporter gene inserted at *URA3*, or NTS1 at the rDNA. Right: Average fluorescence intensities quantified from different strains in the left panel and normalized to the reporter level at *URA3* in WT cells.

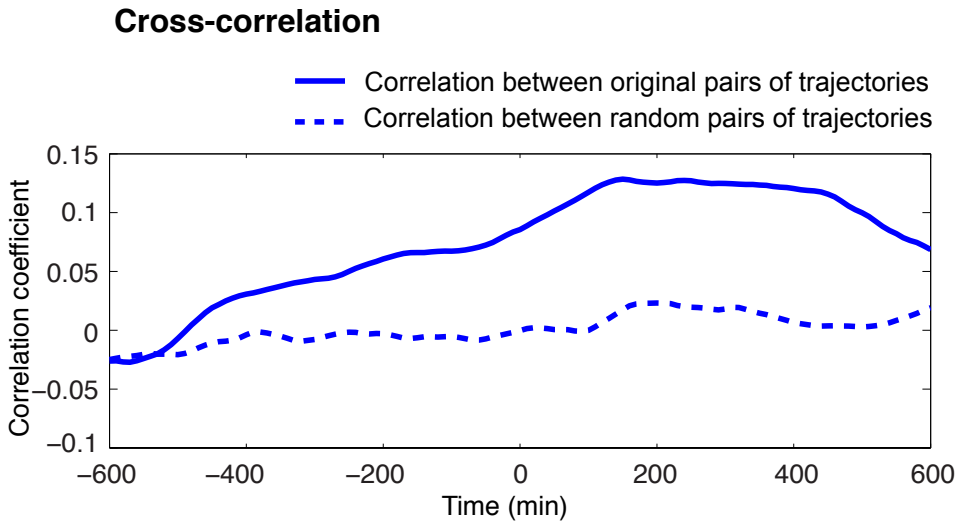

Fig. S2. The cross-correlation between silencing loss in mother cells and their daughter morphologies. To determine the time-dependent relationship between silencing loss in aging mother cells and the occurrence of elongated daughters, we calculated the cross-correlation between silencing reporter fluorescence trajectories of each mother cell (from Fig. 2A) and the morphology change trajectories of its daughters.

The daughter morphology was mapped as a binary variable that is set to "1" when the daughter is elongated and "0" when the daughter is rounded. Because daughter morphology traces are digitalized, we also digitized silencing reporter fluorescence trajectories of mother cells. To this end, we first took the time derivatives of a fluorescence trajectory, and then set positive derivative as 1 (representing the silencing loss state) and negative derivative as -1 (representing the silenced state).

For each pair of mother silencing loss trajectory, MSL (1, 2, … n), and daughter morphology trace i, DM (1, 2, … n), with n time points, we aligned them with a time shift $\Delta\tau$: MSL(i) (1, 2, … n-$\Delta\tau$) and DM(i) (1+$\Delta\tau$, 2+$\Delta\tau$, … n) for $\Delta\tau \geq 0$, or MSL(i) (1+|$\Delta\tau$|, 2+|$\Delta\tau$|, … n) and DM(i) (1, 2, … n-|$\Delta\tau$|) for $\Delta\tau < 0$. For each $\Delta\tau$, we concatenated all mother silencing loss trajectories into one long silencing loss trajectory and all daughter morphology trajectories into one long morphology trajectory. We then calculated the correlation coefficient between the concatenated pair of mother-daughter trajectories with the shift $\Delta\tau$ using Matlab function corrcoef.

To provide a control for this cross correlation analysis, we disrupted the original pairing between mother silencing loss and daughter morphology trajectories. Instead of pairing each mother silencing loss trajectory with its own daughter morphology trajectory, we randomly paired mother silencing loss trajectories with daughter morphology trajectories, and then performed the same cross correlation calculation for the concatenated mother trajectory and "randomly reshuffled" daughter trajectory (the dashed line).

The correlation analysis revealed a ~140 min time lag between silencing loss and daughter morphology trajectories, indicating a time delay between the changes at the molecular level – the occurrence of silencing loss and the changes at the phenotypic level – the production of elongated daughters during the aging process.

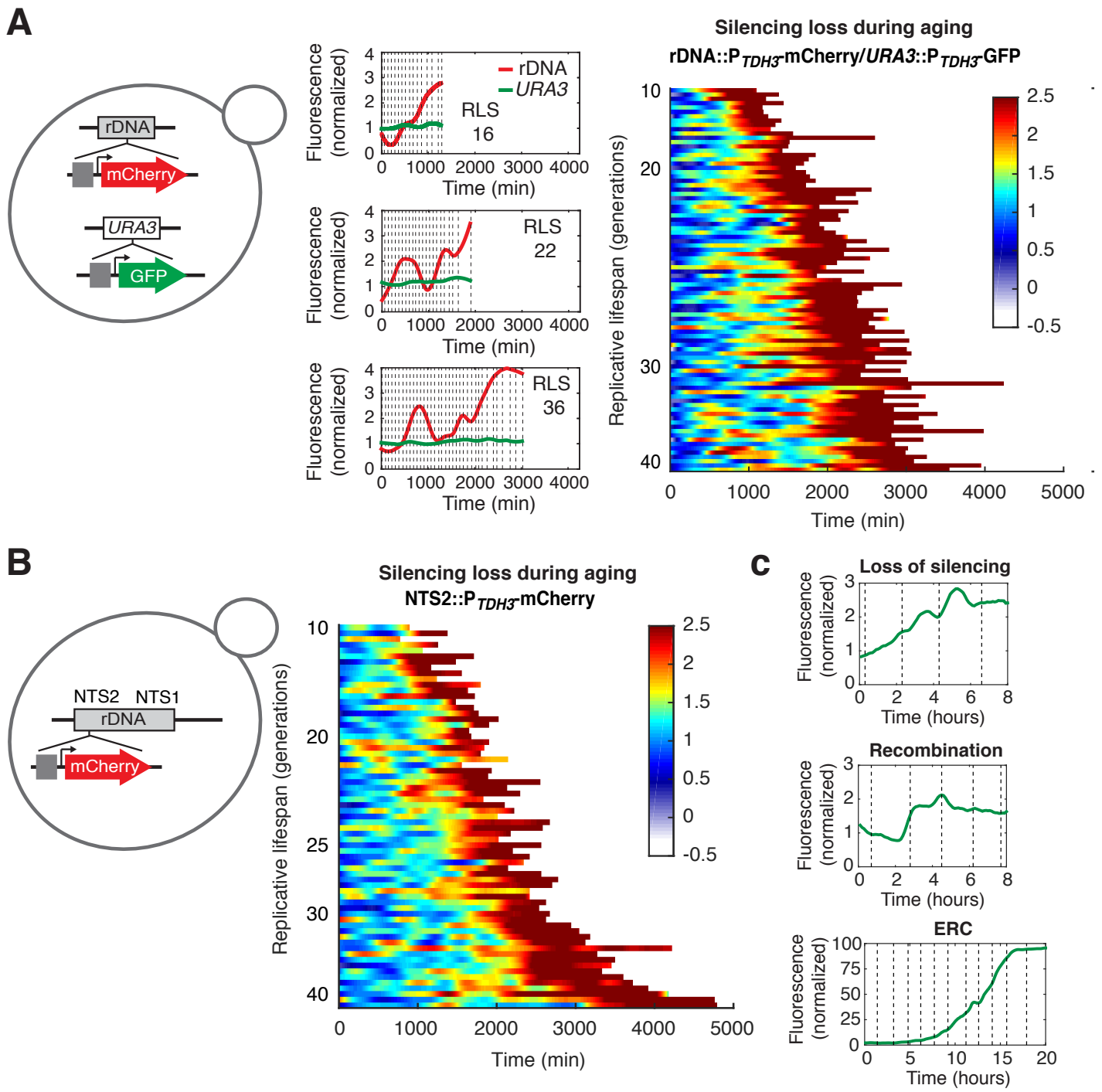

Fig. S3. Validation of the silencing reporter dynamics during aging. (A) Dynamic patterns of reporter fluorescence are not caused by age-associated global effects on gene expression. Left: A schematic illustrating the dual-color strain, in which mCherry under the *TDH3* promoter is inserted at the NTS1 region at rDNA and GFP under the same promoter is inserted at *URA3*. Middle: Representative single-cell time traces of the dual-color cells throughout their lifespans. Each plot shows the time traces of NTS1-mCherry and *URA3*-GFP in a single cell. Vertical dashed lines represent division times of the cell, in which the distance between two adjacent dashed lines indicates the cell cycle duration. The number of dashed lines in each trace represents the cell's lifespan. Reporter fluorescence is normalized to the baseline level. Right: Single-cell density map trajectories for rDNA-mCherry divided by *URA3*-GFP in the same cells (cells aging with elongated daughters). Because the expression of *URA3*-GFP reporter shows little change during aging, the density map trajectories of rDNA-mCherry, normalized by *URA*3-GFP in the same cells, show similar patterns to those observed in Fig. 2A. **(B)** Dynamic patterns of silencing loss are not specific to the NTS1 region of rDNA. Left: A schematic illustrating the strain in which mCherry under the *TDH3* promoter is inserted at the NTS2 region at rDNA. Right: Single-cell density map trajectories for NTS2-mCherry during aging. Silencing loss at the NTS2 region shows similar patterns to those observed for the NTS1 region. **(C)** Representative single-cell time traces for loss of silencing, recombination, or ERC of the reporter gene. Top: Loss of silencing features a gradual fluorescence increase. Middle: Recombination features a fast 2-fold fluorescence change in one cell division and at the same time the daughter cell from that cell division stably loses the reporter gene. Bottom: ERC features a drastic exponential fluorescence increase until detection saturation.

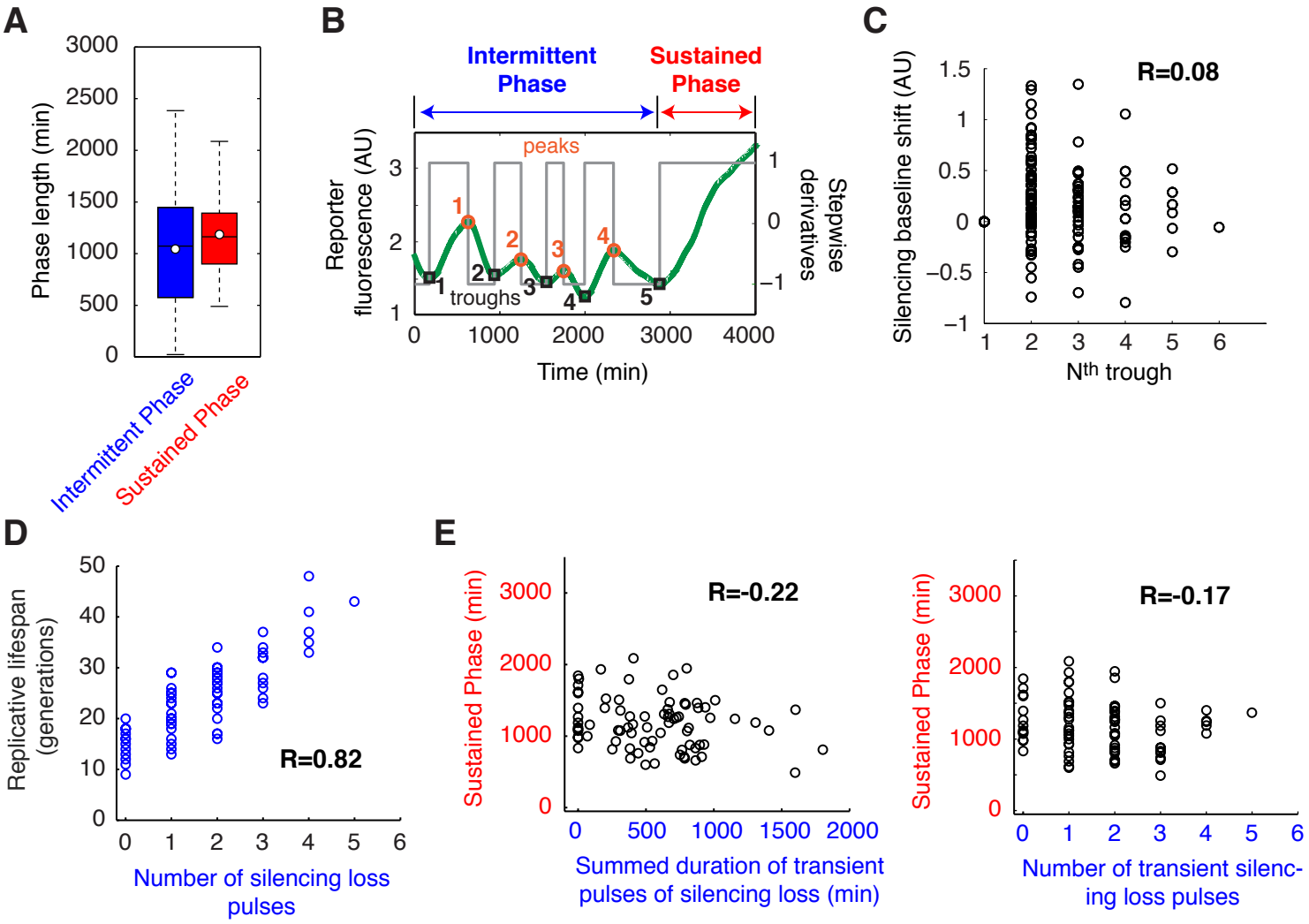

Fig. S4. Additional quantification of silencing loss dynamics in single cells. (A) A boxplot showing the distributions of (blue) Intermittent Phase length and (red) Sustained Phase length in single cells. Single-cell data are from Fig. 2A. In the plot, the bottom and top of the box are first (the 25th percentile of the data, q1) and third quartiles (the 75th percentile of the data, q3); the band inside the box is the median; the white circle is the mean; the whiskers cover the range between q1-1.5 x (q3-q1) and q3+1.5 x (q3-q1). **(B)** A schematic illustrates the identification of peaks (orange circles) and troughs (black squares) within Intermittent Phase in a representative single-cell time trace (green curve). The grey trace is the stepwise derivative trajectory of the time trace. The identification procedure are described in Supplemental Information - *Quantification of single-cell traces*. **(C)** A scatter plot showing the relationship between the baseline shift values of troughs and their sequential positions in time traces. For each time trace, the fluorescence value of each trough is subtracted with the value of the 1st trough to calculate the silencing baseline shift during aging of this cell. The baseline shift value of each trough versus its sequential position (1st, 2nd, 3rd …) in a single-cell time trace was plotted. If the baseline level increases in the majority of cells, we would expect to see a general trend with positive baseline shifts increasing with the trough positions. As shown in the panel, we observed little relationship between baseline shift and trough positions, with a correlation coefficient of 0.08. Therefore, we conclude that sporadic waves of silencing loss show modest effects on the basal silencing level during aging. **(D)** A scatter plot showing the relationship between the number of early silencing loss pulses and final lifespan at the single-cell level. Each circle represents a single cell. Correlation coefficient (R) has been calculated and shown in the plot. **(E)** Sporadic transient waves of silencing loss have little contribution to cell death**.** Left: A scatter plot showing the relationship between the summed duration of sporadic transient silencing loss (summed t1 in Fig. 3b for each cell) and the duration of Sustained Phase preceding cell death (t2 in Fig. 3B for each cell) at the single-cell level. Single-cell data are from Fig. 2A. Each circle represents a single cell. Correlation coefficient (R) has been calculated and shown. Right: A scatter plot showing the relationship between total number of sporadic transient waves of silencing loss and the duration of Sustained Phase at the single-cell level. If transient pulses of silencing loss can contribute to cell death, additively to sustained silencing loss, cells with more transient pulses would exhibit shorter Sustained Phase of silencing loss before cell death. In fact, the summed duration (or number) of transient pulses of silencing loss show very poor correlation with the length of Sustained Phase, suggesting little contribution to cell death.

Fig. S4

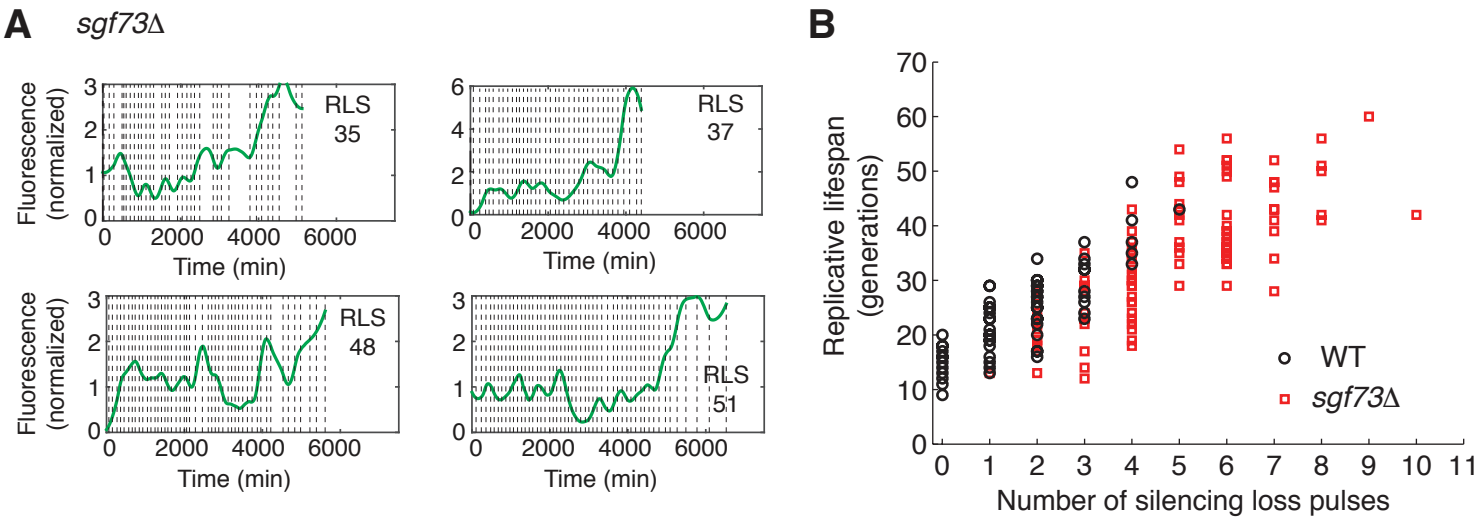

Fig. S5. Dynamics of silencing loss in *sgf73*Δ. (A) Representative single-cell time traces of silencing loss in *sgf73*Δ. Vertical dashed line represents each division time of the cell, in which the distance between two adjacent dashed lines indicates the cell cycle length. Reporter fluorescence is normalized to the baseline level. **(B)** A scatter plot showing the relationship between the number of early silencing loss pulses and final lifespan at the single-cell level for WT (black circles) and *sgf73*Δ (red squres). Each symbol represents a single cell.

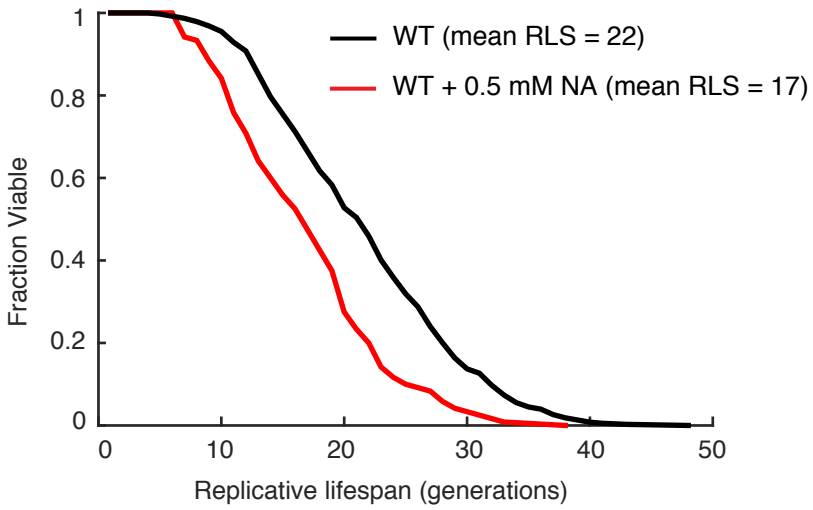

Fig. S6. A constant treatment of 0.5 mM NA shortens the lifespan. Lifespan curves have been shown for WT cells with (red solid curve) or without (black solid curve) 0.5 mM NA treatment. The NA concentration used in Fig. 5D (2.5 mM) is lower than that used in most previous studies (5 mM)(Anderson et al, *Nature*, 2003; Bitterman et al, *JBC*, 2002). Here, the dosage of NA has been further reduced by 5 times to 0.5 mM, which is the lowest dose that can be found in the literature (Mei et al, *PLoS Biol*, 2015). A constant treatment of this very low dose of NA also resulted in a significantly shortened lifespan.

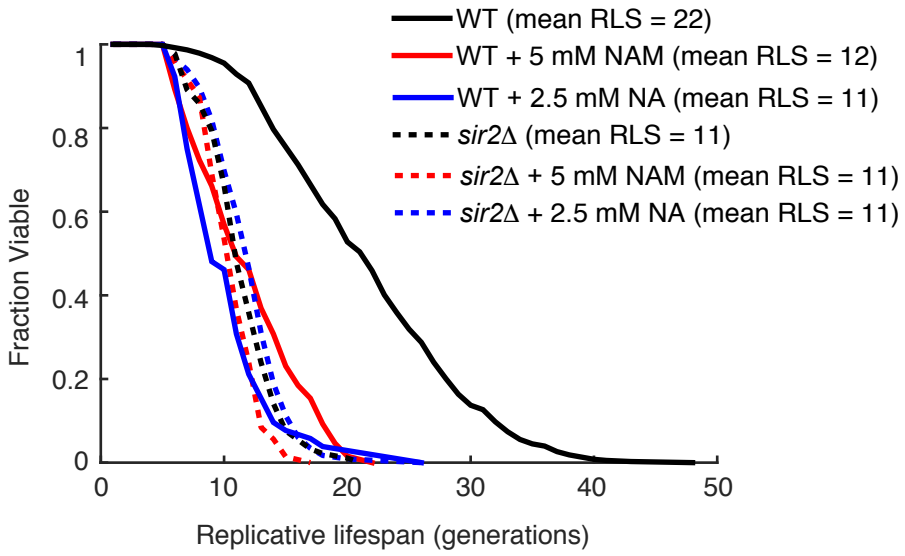

Fig. S7. The effects of NAM and NA treatments on lifespan are mediated through Sir2. Lifespan curves have been shown for WT cells with 5 mM NAM (red solid curve) or 2.5 mM NA (blue solid curve) treatments, or in normal growth medium (black solid curve), as well as *sir2*Δ cells with 5 mM NAM (red dashed curve) or 2.5 mM NA (blue dashed curve) treatments, or in normal growth medium (black dashed curve).

Fig. 2A

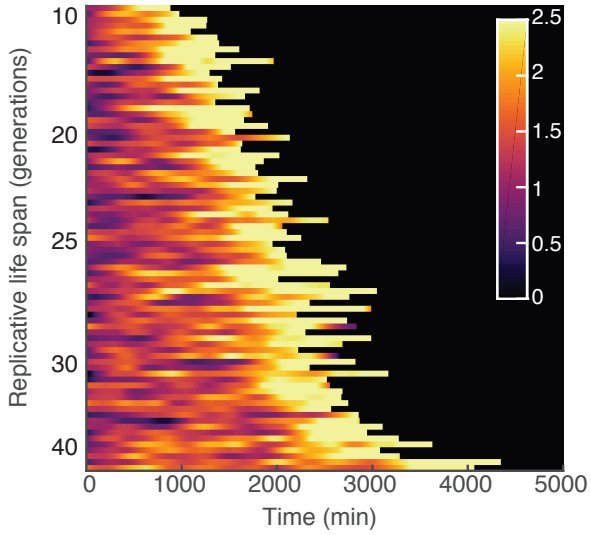

Fig. 2B

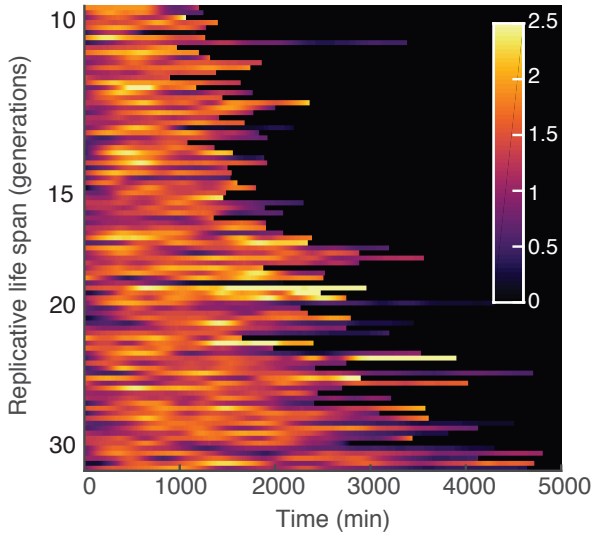

Fig. 5A

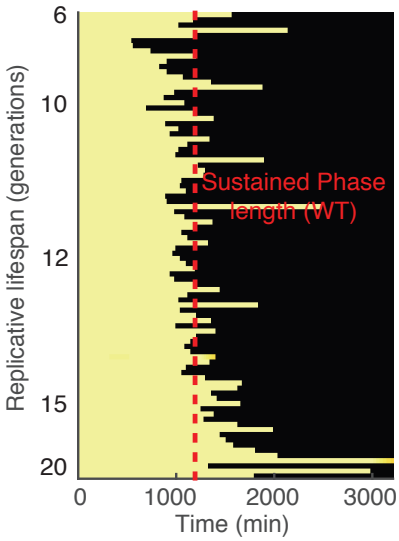

Fig. 5B

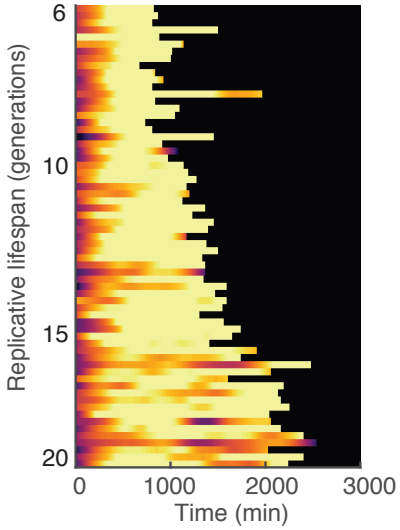

Fig. 5C

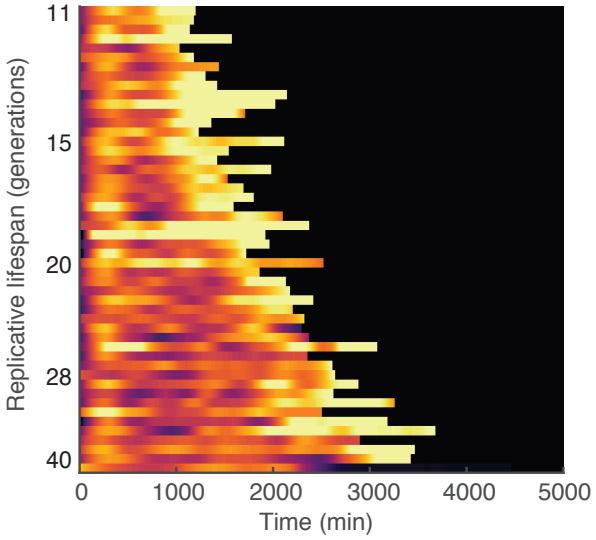

Fig. 5D

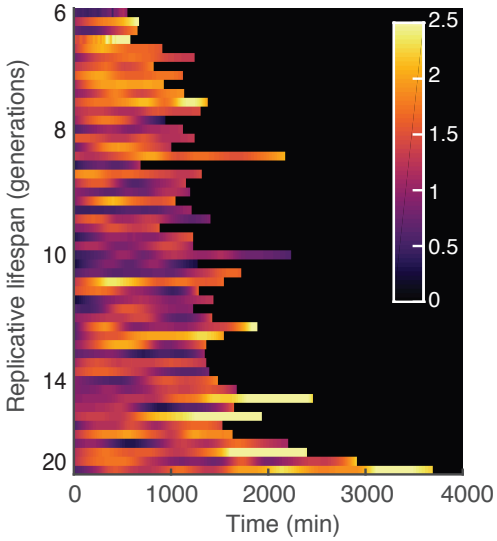

Fig. S8. The 'inferno' version of all the heatmaps shown in the main figures. The 'inferno' color map is used as a perceptually uniform sequential colormap to aid in interpretation of the intensity information even when printed or viewed in grayscale.